Gait Generation of a 10-DOF Humanoid Robot on Deformable Terrain Based on Spherical Inverted Pendulum Model

Sunil Gora *
Department of
Mechanical Engineering,
Indian Institute of Technology, Kanpur,
Uttar Pradesh, India, 208016
Email: sunilg@iitk.ac.in

Shakti S Gupta
Department of Mechanical Engineering,
Indian Institute of Technology, Kanpur,
Uttar Pradesh, India, 208016
Email: ssgupta@iitk.ac.in

Ashish Dutta
Department of Mechanical Engineering
Indian Institute of Technology, Kanpur
Uttar Pradesh, India, 208016
Email: adutta@iitk.ac.in

ABSTRACT

Gait generation of a humanoid robot on a deformable terrain is a complex problem as the foot and terrain interaction and terrain deformation have to be included in the dynamics. In order to simplify the dynamics of walk on deformable terrain, we used a spherical inverted pendulum (SIP) to represent the single support phase, in which the effect of terrain deformation is represented by a spring and damper contact model. The impact model for leg transition is derived from angular momentum conservation. In order to minimize the energy loss due to impact, the double support phase is modeled as a suspended pendulum. Based on the motion of the SIP model, the hip and leg trajectories of a 10-DOF humanoid robot are generated. The joint trajectories of the robot are obtained from inverse kinematics. The motion of the center of mass is analyzed by inverse dynamics of a floating-base robot. The proposed gait generation method has been experimentally validated using a Kondo KHR-3HV humanoid robot on deformable terrain. The results show that the humanoid can effectively track the trajectories of the SIP model.

*Address all correspondence to this author.

1 INTRODUCTION

The zero moment point (ZMP) based walking of humanoid robot on flat hard terrain [1, 2], inclined terrain [3], and stairs [4] is extensively studied in the literature. Robot walking on uneven terrain is addressed using footstep planning with an optimization-based walking controller [5] and ground force control for terrain uncertainties [6]. The legged robots can walk in outdoor environments [7] and have reported challenges in gait selection for walking on deformable terrain [8, 9]. For walking on deformable terrain, Hashimoto et al. [10] analyzed the human gait and stabilized the lateral center of mass (COM) motion by the ankle torque according to the measured attitude angle of the robot. The terrain deformation increased the double support phase, which is handled by adjusting the contact forces based on the zero moment point position. Mesesan et al. [11] also used a damping wrench to stabilize the stance foot on deformable terrain. However, the trajectory generation using the divergent component of motion (DCM) is based on rigid contact assumption.

On the other hand, Ding et al. [12] studied the foot-terrain interaction modeling for different terrains. Zheng et al. [8] utilized the foot-terrain interaction model to design a step-over gait for humanoid walking with small terrain deformation, whereas ski-type quadruped gait is proposed for robust walking on highly deformable surfaces. The effect of terrain deformation on the floating-base dynamics of biped is analyzed in [13]. Based on the floating-base dynamics with foot-terrain interaction, the leg trajectories are modified to stabilize the stance leg foot. The change in the orientation of the floating base is shown to be due to the varying center of pressure over the period of walking. The rotation of the foot reduces the effective support area and also results in swing leg impact during foot landing. The effective support area and stability region criterion on deformable granular terrain are analyzed in [14].

For reduced-order dynamics of linear inverted pendulum mode (LIPM), the motion of the COM is constrained in a plane [15]. For smooth trajectory, Shibuya et al. [16] modeled the double support phase (DSP) as a pendulum suspended at a virtual supporting point (VSP), which is called linear pendulum mode (LPM). Xie et al. [17] extended the LIPM and LPM for three-dimensional walking with the DSP. The constrained motion of the COM in LIPM and LPM can be dynamically unstable and energy-inefficient for walking on deformable terrain. The passive walking model, such as the nonlinear inverted pendulum (NIP) [18] can incorporate terrain deformation using the foot-terrain contact model [19]. For three-dimensional walking on deformable terrain, spherical inverted pendulum (SIP) model with foot-terrain contact model is presented in this paper. The energy-efficient walking of passive walkers is prominently due to the design of the leg such that impact loss is minimized [20]. For energy-efficient passive walking gait, the impact loss can be minimized by gradually changing contact forces in the double support phase. The leg support transition with finite double support phase for three-dimensional walking on deformable terrain is not available in the literature to the best of the author's knowledge.

In this work, SIP model for simplified dynamics of the robot in the single support phase and the suspended nonlinear pendulum model in the double support phase are used for gait generation of the humanoid robot on deformable terrain. The salient contributions of this work are as follows:

1. Impact modeling of leg transition using a spherical inverted pendulum and simplified dynamics in double support phase as a suspended nonlinear pendulum for three-dimensional motion of the robot,
2. Three-dimensional walking pattern generation using the motion of the spherical inverted pendulum in single support phase on deformable terrain,
3. Gait generation of 10-DOF humanoid robot using the motion of the reduced-order dynamics model for walking on deformable terrain.

This paper is organized as follows: In Sec. 2, the dynamics of the 10-DOF humanoid robot and spherical inverted pendulum model is presented. In Sec. 3, the impact modeling for leg transition and the simplified dynamics in the double support phase as a suspended nonlinear pendulum is shown. The gait generation of a 10-DOF humanoid robot using the motion of the simplified model, and the simulation and experimental results are discussed in Sec. 4. Finally, the conclusions are given in Sec. 5.

2 DYNAMICS OF 10-DOF HUMANOID ROBOT AND SPHERICAL INVERTED PENDULUM MODEL

In this section, the kinematics and dynamics of the 10-DOF humanoid robot and the simplified dynamics model of the spherical pendulum is discussed.

2.1 Kinematic and dynamic modeling of 10-DOF humanoid robot

The 10-DOF humanoid robot with a floating-base attached to the hip link center is shown in Fig. 1. The generalized joint coordinates of the robot are written as

$$\boldsymbol{q} = \begin{bmatrix} \boldsymbol{q}_0 \\ \boldsymbol{q}_\theta \end{bmatrix}, \tag{1}$$

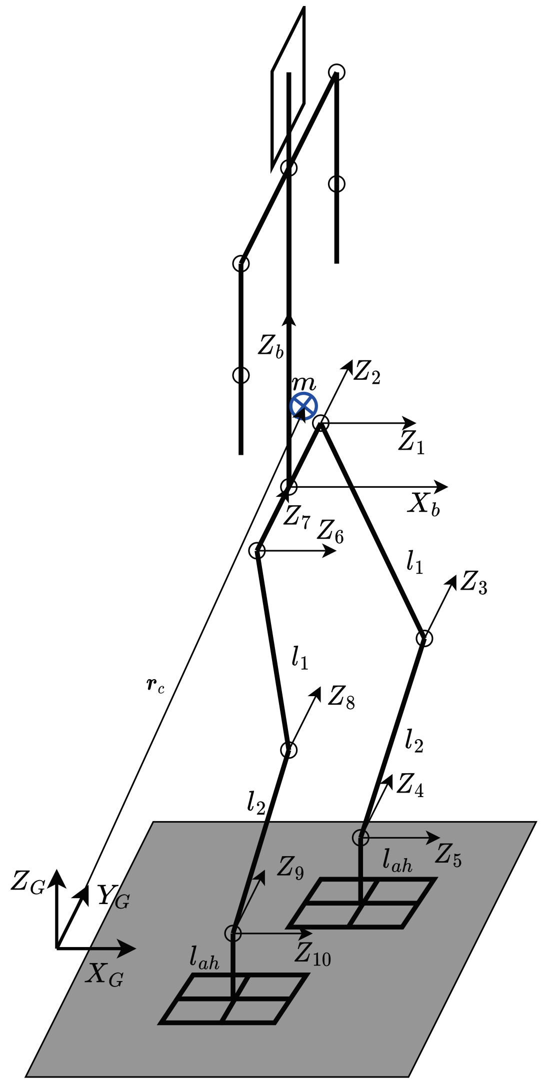

Fig. 1: 10-DOF humanoid robot

where,

$$\boldsymbol{q}_0 = \begin{bmatrix} z_0 \; y_0 \; x_0 \; \theta_{x0} \; \theta_{y0} \; \theta_{z0} \end{bmatrix}^T, \tag{2}$$

$$\boldsymbol{q}_\theta = \begin{bmatrix} \theta_1 \; \theta_2 \; \cdots \; \theta_{10} \end{bmatrix}^T. \tag{3}$$

Here, $\boldsymbol{q}_0 \in \mathbb{R}^{6\times1}$ denotes the vector of unactuated virtual joint coordinates of the floating-base frame attached to the hip link and $\boldsymbol{q}_\theta \in \mathbb{R}^{10\times1}$ denotes the vector of actuated joint coordinates of the robot. The equations of motion of the 10-DOF humanoid robot [21] are written as

$$\begin{bmatrix} \boldsymbol{I}_0 & \boldsymbol{I}_{0\theta} \\ \boldsymbol{I}_{0\theta}^T & \boldsymbol{I}_\theta \end{bmatrix} \begin{bmatrix} \ddot{\boldsymbol{q}}_0 \\ \ddot{\boldsymbol{q}}_\theta \end{bmatrix} + \begin{bmatrix} \boldsymbol{c}_0 \\ \boldsymbol{c}_\theta \end{bmatrix} = \begin{bmatrix} \boldsymbol{0} \\ \boldsymbol{\tau}_\theta \end{bmatrix} + \begin{bmatrix} \boldsymbol{\tau}_{e_0} \\ \boldsymbol{\tau}_{e_\theta} \end{bmatrix}. \tag{4}$$

Here, $\boldsymbol{I}_0 \in \mathbb{R}^{6\times 6}$ is the inertia matrix of the floating-base, $\boldsymbol{I}_\theta \in \mathbb{R}^{10\times 10}$ is the inertia matrix of the links, $\boldsymbol{I}_{0\theta} \in \mathbb{R}^{6\times 10}$ is the coupling inertia matrix, $\boldsymbol{c}_0 \in \mathbb{R}^{6\times 1}$ and $\boldsymbol{c}_\theta \in \mathbb{R}^{10\times 1}$ are the vectors of position and velocity dependent terms associated with the base and links, respectively, $\boldsymbol{\tau}_\theta \in \mathbb{R}^{10\times 1}$ is the joint torques vector. The torque components $\boldsymbol{\tau}_{e_0} \in \mathbb{R}^{6\times 1}$ and $\boldsymbol{\tau}_{e_\theta} \in \mathbb{R}^{10\times 1}$ due to contact forces are expressed as

$$\boldsymbol{\tau}_{e_0} = \sum_{i=1}^{2} \boldsymbol{J}_{i_0}^T \boldsymbol{w}_i, \tag{5}$$

$$\boldsymbol{\tau}_{e_\theta} = \sum_{i=1}^{2} \boldsymbol{J}_{i_\theta}^T \boldsymbol{w}_i, \tag{6}$$

where, $\boldsymbol{J}_{i_0} \in \mathbb{R}^{6\times 6}$ and $\boldsymbol{J}_{i_\theta} \in \mathbb{R}^{6\times 10}$ are the Jacobian matrices of the base and links, respectively, $\boldsymbol{w}_i \in \mathbb{R}^{6\times 1}$ is the vector of moments and forces acting at the i^{th} ankle due to contact force [22].

2.2 Spherical inverted pendulum model

The nonlinear inverted pendulum (NIP) model for robot walking in a plane is studied in the literature [19]. This reduced-order model extended for three-dimensional motion of humanoid robot on deformable terrain is presented in this section. The dynamics of the humanoid robot is simplified as a spherical inverted pendulum (SIP) model shown in Fig. 2. The desired center of pressure (COP) position for the stance leg foot on deformable terrain is at the center of the foot, which is considered as the contact point in the SIP model. The mass of the SIP is m and the mass moment of inertia matrix is denoted by $\boldsymbol{I}$. The distance between the center of mass (COM) and the contact point is l. The orientation of the pendulum is described by the Euler angles θ_x and θ_y, which are the angles of rotation about the current x and y-axis, respectively. The corresponding rotation matrices are denoted by $\boldsymbol{R}_{\theta_x}$ and $\boldsymbol{R}_{\theta_y}$. The position vector of the COM of the SIP $\boldsymbol{r}_c = [x_c, y_c, z_c]^T$ in terms of the position vector of the contact point $\boldsymbol{r} = [x, y, z]^T$ and the orientation of

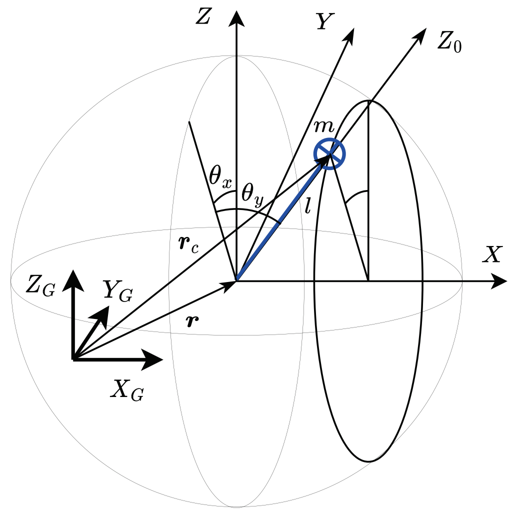

Fig. 2: Spherical inverted pendulum model

the pendulum can be written as

$$\boldsymbol{r}_c = \boldsymbol{r} + \boldsymbol{R}_{\theta_x}\boldsymbol{R}_{\theta_y}\begin{bmatrix}0, 0, l\end{bmatrix}^T. \tag{7}$$

The substitution of the expression of rotation matrices in Eq. (7) gives

$$\begin{bmatrix} x_c \\ y_c \\ z_c \end{bmatrix} = \begin{bmatrix} x \\ y \\ z \end{bmatrix} + l \begin{bmatrix} \sin\theta_y \\ -\cos\theta_y \sin\theta_x \\ \cos\theta_y \cos\theta_x \end{bmatrix}. \tag{8}$$

The generalized joint coordinates of the SIP are given as

$$\boldsymbol{q}_p = \begin{bmatrix} x \; y \; z \; \theta_x \; \theta_y \end{bmatrix}^T. \tag{9}$$

The equations of motion of the SIP can be written as

$$\boldsymbol{I}_p \ddot{\boldsymbol{q}}_p + \boldsymbol{c}_p = \boldsymbol{J}_p^T \boldsymbol{f}_p, \tag{10}$$

where, $\boldsymbol{I}_p \in \mathbb{R}^{5\times5}$ is the inertia matrix, $\boldsymbol{c}_p \in \mathbb{R}^{5\times1}$ is the vector of the Coriolis, centrifugal and gravitational forces, and $\boldsymbol{J}_p \in \mathbb{R}^{3\times5}$ is the Jacobian matrix, the expressions of which are given in Appendix A. $\boldsymbol{f}_p \in \mathbb{R}^{3\times1}$ is the vector of the contact forces. The contact forces are modeled using a spring and a damper [19]. The normal contact force f_n is given by

$$f_n = \begin{cases} -k_n\delta_n - c_n\dot{\delta}_n, & \delta_n < 0 \text{ and } \dot{\delta}_n < 0, \\ -k_n\delta_n, & \delta_n < 0 \text{ and } \dot{\delta}_n \geq 0, \\ 0, & \delta_n \geq 0. \end{cases} \tag{11}$$

Here, δ_n and $\dot{\delta}_n$ are the displacement and relative velocity of the contact point on the pendulum with respect to the undeformed surface of the ground in the normal direction. k_n and c_n are the terrain stiffness and damping, respectively. The relative position and velocity vector of the contact point in the tangential plane are $\boldsymbol{\delta}_t$ and $\dot{\boldsymbol{\delta}}_t$, respectively. The tangential force $\boldsymbol{f}_t$ is given by

$$\boldsymbol{f}_t = \begin{cases} -k_t\boldsymbol{\delta}_t - c_t\dot{\boldsymbol{\delta}}_t, & \|\boldsymbol{f}_t\| < \mu f_n, \\ \frac{\mu f_n}{\|-k_t\boldsymbol{\delta}_t - c_t\dot{\boldsymbol{\delta}}_t\|}(-k_t\boldsymbol{\delta}_t - c_t\dot{\boldsymbol{\delta}}_t), & \|\boldsymbol{f}_t\| \geq \mu f_n. \end{cases} \tag{12}$$

Here, k_t and c_t are the terrain stiffness and damping in the tangential direction, and μ is the coefficient of friction, which is assumed to be sufficient for the No-slip condition. The undeformed surface of the terrain is considered as a reference, which is a simplification of the contact model. Also, the contact model is simplified to incorporate only positive force components in the normal direction. This is based on the observation that the robot's foot is not clamped to the deformable polyurethane (PU) foam sheet, so it can only exert positive normal force on the foot.

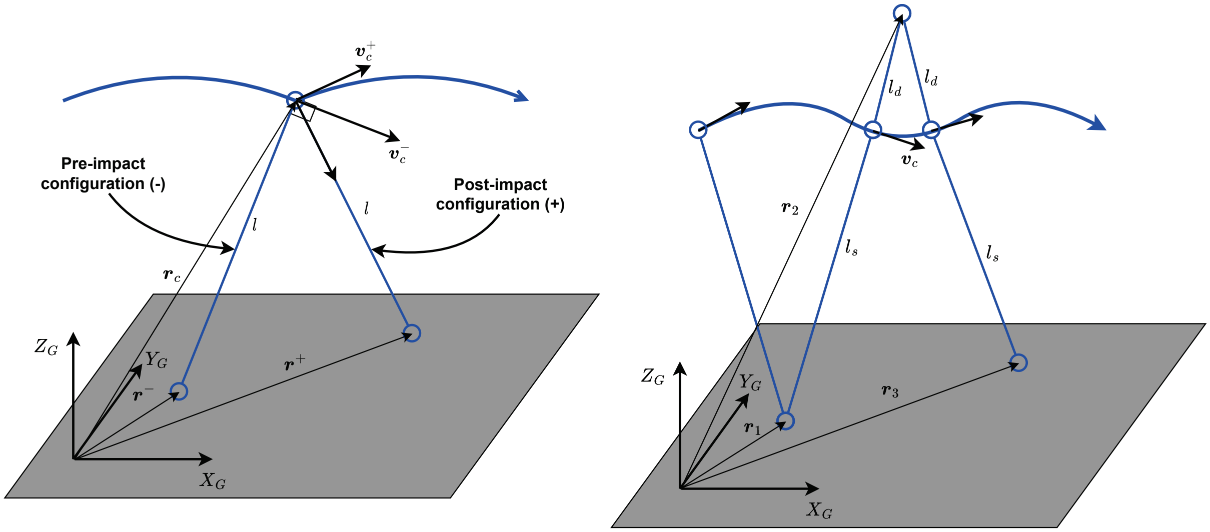

(a) Double support phase with instantaneous leg transition

(b) Leg transition with finite double support phase

Fig. 3: Impact model for leg transition

3 LEG TRANSITION OF SIP MODEL

Footstep planning of the biped robot is crucial for a dynamically stable and energy-efficient walking gait. The energy loss due to impact varies with the position of foot placement [19]. In this section, we first derive the expression of energy loss due to impact for the double support phase with instantaneous leg transition, which is shown in Fig. 3a. To minimize the impact, the motion in the double support phase is described using a suspended pendulum as shown in Fig. 3b. Footstep planning with finite double support phase and three-dimensional walking pattern generation of the COM are presented in the subsequent parts of this section.

3.1 Impact modeling of SIP

The dynamics of the SIP is described in Eq. (10). For leg transition with instantaneous DSP, the velocity and acceleration of the stance leg foot contact point can be neglected in the SIP model. The pre-impact and post-impact configurations are shown in Fig. 3a. The position vector of the COM during leg transition is $\boldsymbol{r}_c = [x_c, y_c, z_c]^T$. The pre-impact velocity vector of the COM is $\boldsymbol{v}_c^- = [\dot{x}_c^-, \dot{y}_c^-, \dot{z}_c^-]^T$. The pre-impact and post-impact contact position vectors are $\boldsymbol{r}^- = [x^-, y^-, z^-]^T$ and $\boldsymbol{r}^+ = [x^+, y^+, z^+]^T$, respectively. The pre-impact angular momentum about the post-impact contact point is

$$\boldsymbol{L}^{-} = (\boldsymbol{r}_c - \boldsymbol{r}^{+}) \times m\boldsymbol{v}_c^{-}. \tag{13}$$

The post-impact velocity vector of the COM is $\boldsymbol{v}_c^{+} = [\dot{x}_c^{+}, \dot{y}_c^{+}, \dot{z}_c^{+}]^T$. The post-impact angular momentum about the post-impact contact point is

$$\boldsymbol{L}^{+} = (\boldsymbol{r}_c - \boldsymbol{r}^{+}) \times m\boldsymbol{v}_c^{+}. \tag{14}$$

From motion constraint, the post-impact velocity vector is perpendicular to the radial direction, i.e.,

$$(\boldsymbol{r}_c - \boldsymbol{r}^{+})^T \boldsymbol{v}_c^{+} = 0. \tag{15}$$

Using Eq. (15) and the conservation of angular momentum, i.e., $\boldsymbol{L}^{-} = \boldsymbol{L}^{+}$, the post-impact velocity vector can be written as

$$\boldsymbol{v}_c^{+} = \boldsymbol{\Phi}\boldsymbol{v}_c^{-}. \tag{16}$$

Here, $\boldsymbol{\Phi} \in \mathbb{R}^{3\times 3}$ is the impact map matrix. The components of matrix $\boldsymbol{\Phi}$ are

$$\Phi_{11} = 1 - \frac{(x_c - x^{+})^2}{(\boldsymbol{r}_c - \boldsymbol{r}^{+})^T(\boldsymbol{r}_c - \boldsymbol{r}^{+})}, \tag{17}$$

$$\Phi_{22} = 1 - \frac{(y_c - y^{+})^2}{(\boldsymbol{r}_c - \boldsymbol{r}^{+})^T(\boldsymbol{r}_c - \boldsymbol{r}^{+})}, \tag{18}$$

$$\Phi_{33} = 1 - \frac{(z_c - z^{+})^2}{(\boldsymbol{r}_c - \boldsymbol{r}^{+})^T(\boldsymbol{r}_c - \boldsymbol{r}^{+})}, \tag{19}$$

$$\Phi_{12} = \Phi_{21} = -\frac{(x_c - x^+)(y_c - y^+)}{(\boldsymbol{r}_c - \boldsymbol{r}^+)^T(\boldsymbol{r}_c - \boldsymbol{r}^+)}, \tag{20}$$

$$\Phi_{13} = \Phi_{31} = -\frac{(x_c - x^+)(z_c - z^+)}{(\boldsymbol{r}_c - \boldsymbol{r}^+)^T(\boldsymbol{r}_c - \boldsymbol{r}^+)}, \tag{21}$$

$$\Phi_{23} = \Phi_{32} = -\frac{(y_c - y^+)(z_c - z^+)}{(\boldsymbol{r}_c - \boldsymbol{r}^+)^T(\boldsymbol{r}_c - \boldsymbol{r}^+)}. \tag{22}$$

The magnitude of energy loss due to impact is

$$\Delta E = \frac{1}{2}m(\boldsymbol{v}_c^-)^T[\mathbf{1} - \boldsymbol{\Phi}^T\boldsymbol{\Phi}]\boldsymbol{v}_c^-. \tag{23}$$

By substituting the expression of $\boldsymbol{\Phi}$ in Eq. (23), we get

$$\Delta E = \frac{1}{2}m\frac{((\boldsymbol{r}_c - \boldsymbol{r}^+)^T\boldsymbol{v}_c^-)^2}{(\boldsymbol{r}_c - \boldsymbol{r}^+)^T(\boldsymbol{r}_c - \boldsymbol{r}^+)}. \tag{24}$$

It is evident from Eq. (24) that the magnitude of energy loss is proportional to the dot product of the pre-impact velocity vector of the COM and the position vector of the COM with respect to the post-impact contact position. Hence, the energy loss due to impact is zero when both vectors are perpendicular to each other, which means the post-impact contact point is on the line passing through the COM and the pre-impact contact point.

3.2 Double support phase in leg transition

The double support phase (DSP) with instantaneous leg transition results in energy loss due to impact [23], which can be minimized by smooth leg transition with finite DSP. Shibuya et al. [16] modeled the DSP as linear pendulum mode (LPM) and the single support phase (SSP) as LIPM for smooth trajectory. To describe the motion during finite DSP, a suspended nonlinear pendulum is proposed, which is shown in Fig. 3b. The orthographic views of the three-dimensional motion of the spherical inverted pendulum are shown in Fig. 4. The projections of the 3D motion in the coronal plane (front view), sagittal plane (side view), and transverse plane (top view) are shown in the figure. The spheres with centers S_1 and S_3 represent the motion of the COM in the SSP, and the sphere of center S_2 represents the motion of the COM in the DSP. The positions of the center of spheres S_1 and S_3 are consecutive foot placement positions, whereas the

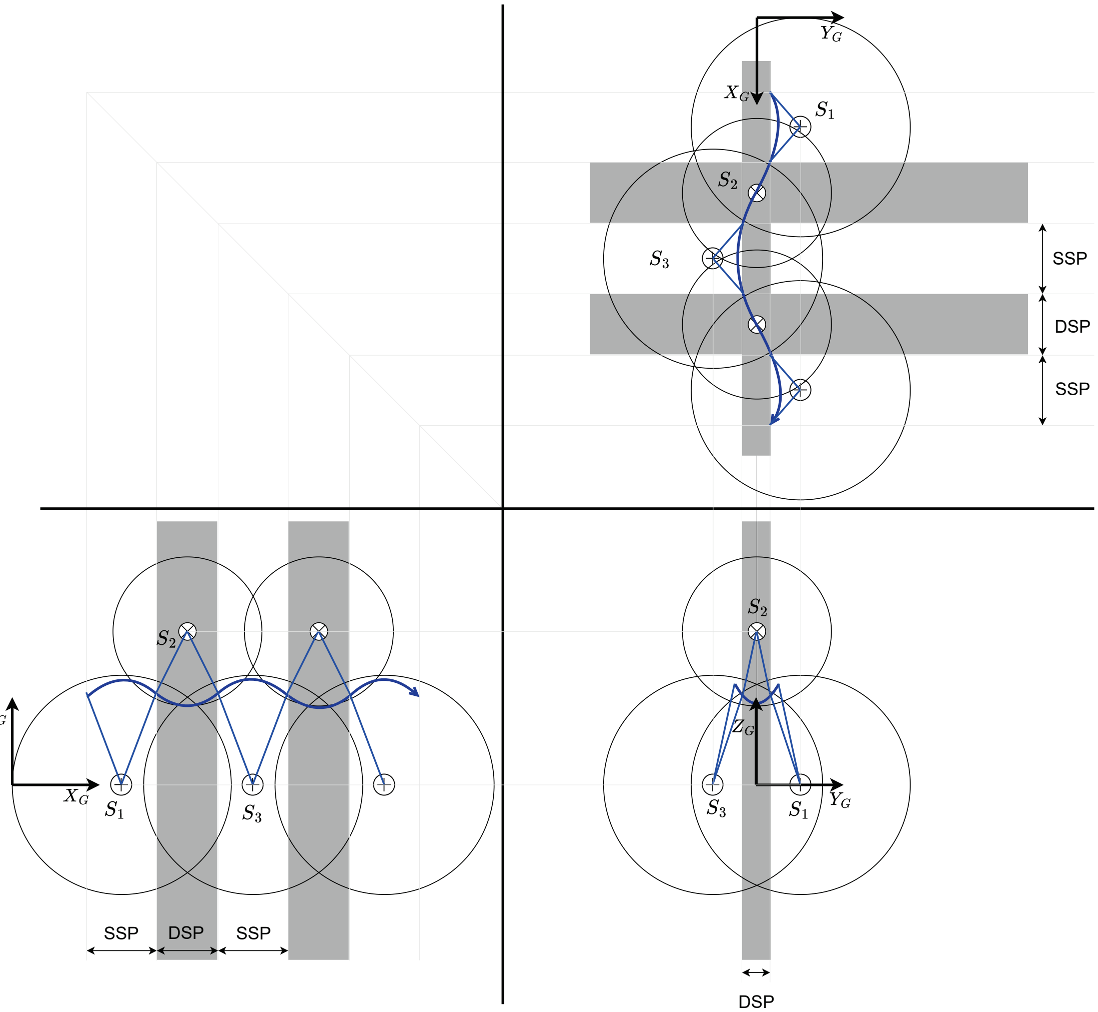

Fig. 4: Orthographic views of the periodic trajectory of the COM

position of the center of sphere S_2 is the virtual supporting point (VSP) [24] for dynamic modeling of the DSP. Let the position vectors of the center of spheres S_1, S_2 and S_3 are $\boldsymbol{r}_1 = [x_1, y_1, z_1]^T$, $\boldsymbol{r}_2 = [x_2, y_2, z_2]^T$ and $\boldsymbol{r}_3 = [x_3, y_3, z_3]^T$, respectively. The spherical pendulum motion in SSP about the contact point S_1 has constant angular momentum about the Z_G-axis, i.e.,

$$(x_c - x_1)\dot{y}_c - (y_c - y_1)\dot{x}_c = \frac{L_z}{m}. \tag{25}$$

The dynamics of the suspended nonlinear pendulum is also described using Eq. (10) as the suspended nonlinear pendulum in DSP is a special case of the spherical pendulum when the motion is in a single plane. The plane of motion of the suspended pendulum is perpendicular to the transverse (X-Y) plane. The angular momentum in the Z_G-direction of the suspended nonlinear pendulum about the contact point S_2 is zero, i.e.,

$$(x_c - x_2)\dot{y}_c - (y_c - y_2)\dot{x}_c = 0. \tag{26}$$

The COP in the SSP is at the center of the sphere S_1. The gradual change of COP from the center of the sphere S_1 to the center of the sphere S_3 using the suspended pendulum in DSP will minimize the energy loss due to impact. If the spheres S_1 and S_2 are tangent to each other, the position of the VSP will be on the line passing through the COM and the center of sphere S_1, which will have zero energy loss due to impact. However, the three-dimensional COM trajectory may not be periodic. Hence, the spheres S_1 and S_2, consisting of the SSP and DSP motion will intersect each other. Let $\Delta\boldsymbol{r} = [\Delta x, \Delta y, \Delta z]^T$ be the position of the COP at the start of the DSP with respect to the center of the sphere S_1, which is the intersection of the line passing from the COM and the center of the sphere S_2 with the terrain. The COP position vector at the start of the DSP is at $\boldsymbol{r}_1 + \Delta\boldsymbol{r}$. For minimum energy loss, the distance between the COP at the end of SSP and the COP at the start of DSP should be minimum. Hence, the position vector $(\Delta x, \Delta y)$ must be perpendicular to the velocity of the COM $(\dot{x}_c, \dot{y}_c)$ in the transverse plane, i.e.,

$$\dot{x}_c\Delta x + \dot{y}_c\Delta y = 0. \tag{27}$$

Also, using Eq. (25), the relation between the position vector, $(\Delta x, \Delta y)$ and L_z can be written as

$$\dot{y}_c\Delta x - \dot{x}_c\Delta y = \frac{L_z}{m}. \tag{28}$$

By solving Eqs. (27) and (28), we get

$$\Delta x = \frac{\dot{y}_c L_z}{m(\dot{x}_c^2 + \dot{y}_c^2)}, \tag{29}$$

$$\Delta y = -\frac{\dot{x}_c L_z}{m(\dot{x}_c^2 + \dot{y}_c^2)}. \tag{30}$$

The equation of the line passing through the COM and the COP at the start of the DSP is

$$\frac{x - x_c}{x_1 + \Delta x - x_c} = \frac{y - y_c}{y_1 + \Delta y - y_c} = \frac{z - z_c}{z_1 + \Delta z - z_c}. \tag{31}$$

As the robot foot is considered flat, the intersection point of this line with the foot support area is at $z = z_1$, i.e., $\Delta z = 0$. Let the length of the suspended pendulum in DSP is l_d, then the position of the center of the sphere S_2 can be obtained as

$$\boldsymbol{r}_2 = \boldsymbol{r}_c - (\boldsymbol{r}_1 + \Delta \boldsymbol{r} - \boldsymbol{r}_c) p_d, \tag{32}$$

where,

$$p_d = \frac{l_d}{\|\boldsymbol{r}_1 + \Delta \boldsymbol{r} - \boldsymbol{r}_c\|}. \tag{33}$$

For periodic walking on flat terrain, the position of the foot placement, i.e., the position of the center of the sphere S_3 can be obtained as

$$x_3 = x_1 + 2(x_2 - x_1), \tag{34}$$

$$y_3 = y_1 + 2(y_2 - y_1), \tag{35}$$

$$z_3 = z_1. \tag{36}$$

The substitution of Eq. (32) in Eq. (24) gives $\Delta E = 0$, which validates that the energy loss due to impact is zero for the proposed leg transition with finite DSP.

3.3 3D walking pattern generation using SIP model in SSP and suspended pendulum in DSP

The dynamics of the SIP model and suspended nonlinear pendulum is described in Eq. (10). The walking pattern of the COM of the robot using the SIP model in the SSP and the suspended nonlinear pendulum in the DSP is shown in Fig. 5a. The terrain parameters used in the simulation are obtained for polyurethane (PU) foam sheet of density $16\,\mathrm{kg/m^3}$. The maximum deformation of $6\,\mathrm{mm}$ under the load of $1.375\,\mathrm{kg}$ with a foot size of $78 \times 122\,\mathrm{mm^2}$ gives the terrain stiffness $2248.125\,\mathrm{N/m}$. The damping ratio ζ is 0.3 [25], and the friction coefficient μ is 0.5. The velocity of the COM with time is plotted in Fig. 5b. The figure shows the continuity of the velocity of the COM with minimized energy loss due to impact. The periodic trajectory of the COM is also evident in the figure.

4 GAIT GENERATION OF 10-DOF ROBOT

The design parameters of the 10-DOF humanoid robot are shown in Table 1. The walking pattern trajectories from the SIP model are used to generate the biped gait. In SSP, the stance leg trajectory is generated using the motion of the contact point of the SIP model. The swing leg trajectory is generated using footstep length and maximum lift of the swing leg foot. The rigid contact assumption of stance leg foot is not valid on deformable terrain. The terrain deformation causes delay during lift and impact during the landing of the swing leg foot in the SSP, which increases the duration of the DSP. This extended DSP is avoided by modifying the leg trajectories using terrain stiffness. The resolution of the contact forces is required for the leg trajectories in the DSP. Let the contact force acting on the suspended pendulum in the DSP is $\boldsymbol{f}_2 = [f_{x2}, f_{y2}, f_{z2}]^T$, which is the resultant of the contact forces acting on both feet, i.e., $\boldsymbol{f}_1 = [f_{x1}, f_{y1}, f_{z1}]^T$ and $\boldsymbol{f}_3 = [f_{x3}, f_{y3}, f_{z3}]^T$. The contact forces $\boldsymbol{f}_1$ and $\boldsymbol{f}_3$ can be obtained by solving the

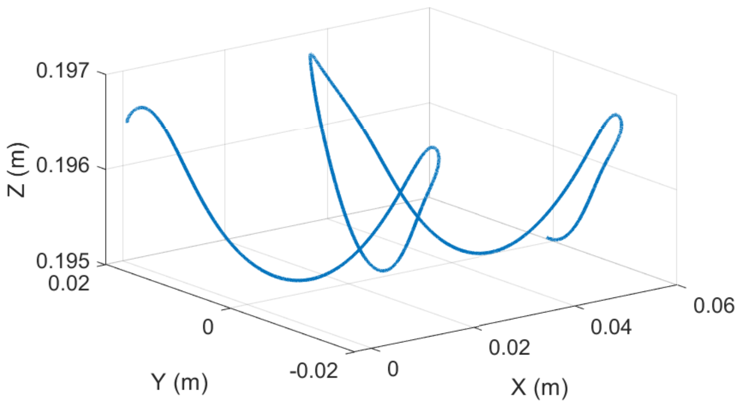

(a) Position of COM

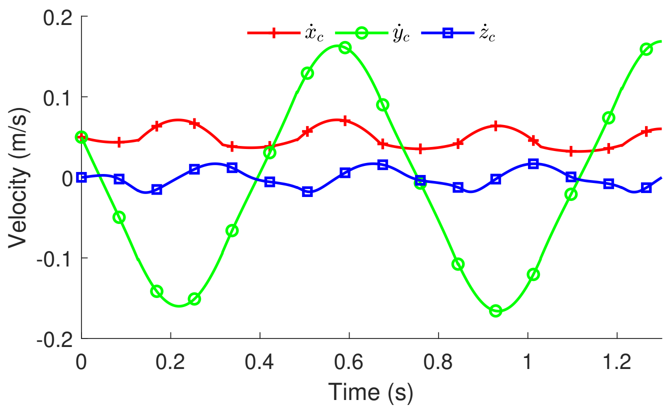

(b) Velocity of COM

Fig. 5: Walking pattern of the COM of the SIP model on flat deformable terrain

optimization problem for a minimum moment about VSP S_2 as

$$\begin{aligned} \min_{\boldsymbol{f}_i} \quad & \Big|\Big| \sum_{i=1,3} (\boldsymbol{r}_i - \boldsymbol{r}_2) \times \boldsymbol{f}_i \Big|\Big|, \\ \text{s.t.} \quad & \sqrt{f_{xi}^2 + f_{yi}^2} \leq \mu f_{zi},\ i = 1,3\ , \\ & f_{x1} + f_{x3} = f_{x2}, \\ & f_{y1} + f_{y3} = f_{y2}, \\ & f_{z1} + f_{z3} = f_{z2}. \end{aligned} \tag{37}$$

From the forces $\boldsymbol{f}_1$ and $\boldsymbol{f}_3$, the leg trajectories in the DSP are generated using the terrain stiffness assuming that the foot ankle velocities and accelerations are negligible. The joint angles are obtained from

Table 1: 10-DOF humanoid robot simulation parameters

Total mass (m)	$1.375\,\mathrm{kg}$
Mass of hip-link	$0.151\,\mathrm{kg}$
Mass of each leg	$0.264\,\mathrm{kg}$
Mass of each arm	$0.124\,\mathrm{kg}$
Mass of upper body	$0.447\,\mathrm{kg}$
Length of thigh (l_1)	$65\,\mathrm{mm}$
Length of shank (l_2)	$65\,\mathrm{mm}$
Height of ankle joint from foot sole (l_{ah})	$26\,\mathrm{mm}$
Maximum lift of swing leg ankle	$15\,\mathrm{mm}$
Size of foot	$78\,\mathrm{mm} \times 122\,\mathrm{mm}$
Normal stiffness of hard terrain	$49\,564.9\,\mathrm{N/m}$
Normal stiffness of deformable terrain	$2248.125\,\mathrm{N/m}$
Damping ratio (ζ)	0.3
Friction coefficient (μ)	0.5
Initial position of COM	$(-0.0035,\, 0.0164,\, 0.1966)\ \mathrm{m}$
Initial position of center of hip-link	$(0,\, 0.0215,\, 0.2161)\ \mathrm{m}$
Initial velocity of center of hip-link	$(0.05,\, 0.05,\, 0)\ \mathrm{m/s}$

the numerical solution of the inverse kinematics with the desired COM position $\boldsymbol{r}_c$ of the SIP model. The forward kinematics of the COM is used to formulate the minimization problem and the leg-ankle trajectories are given as constraints. The optimization problem is formulated as

$$\begin{aligned} \min_{\dot{\boldsymbol{q}}} \quad & ||\boldsymbol{J}_{v_c}\dot{\boldsymbol{q}} - \dot{\boldsymbol{r}}_c||, \\ \text{s.t.} \quad & \begin{bmatrix} \boldsymbol{J}_{\omega_i} \\ \boldsymbol{J}_{v_i} \end{bmatrix} \dot{\boldsymbol{q}} = \begin{bmatrix} \boldsymbol{0} \\ \dot{\boldsymbol{o}}_i \end{bmatrix}, i = 1, 2 \end{aligned} \tag{38}$$

Here, $\boldsymbol{J}_{v_c} \in \mathbb{R}^{3\times16}$ is the Jacobian matrix which maps the rate of joint coordinates to the COM velocity [26]. $\boldsymbol{J}_{v_i} \in \mathbb{R}^{3\times16}$ is the Jacobian matrix which maps the joint velocities to the linear velocities of the i^{th} leg ankle. $\boldsymbol{J}_{\omega_i} \in \mathbb{R}^{3\times16}$ is the Jacobian matrix which maps the joint velocities to the angular velocities of the i^{th} leg ankle. $\dot{\boldsymbol{o}}_i \in \mathbb{R}^{3\times1}$ is the linear velocity vector of the i^{th} leg ankle and $\boldsymbol{0}^{3\times1}$ is the zero vector. The joint

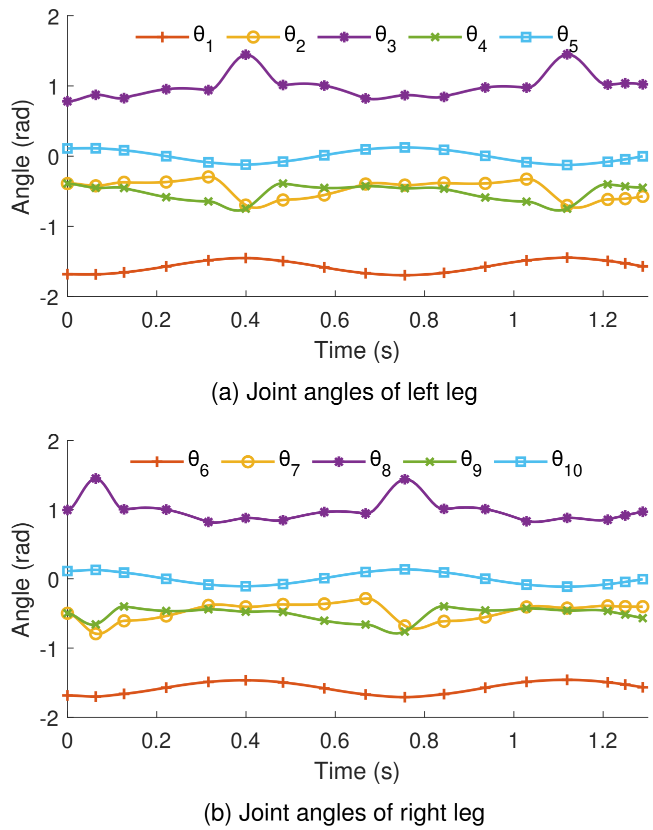

Fig. 6: Joint trajectories for walking on deformable terrain

trajectories obtained for the legs are shown in Fig. 6. Using Eq. (4), the floating-base accelerations are obtained as

$$\ddot{\boldsymbol{q}}_0 = \boldsymbol{I}_0^{-1}(\boldsymbol{\tau}_{e_0} - \boldsymbol{I}_{0\theta}\ddot{\boldsymbol{q}}_\theta - \boldsymbol{c}_0). \tag{39}$$

The floating-base accelerations are integrated using MATLAB ODE solver 'ode45'. The time taken for 1.3 seconds of simulation on Intel core i5-4460 3.20GHz processor is 161.7 seconds. The simulation of the robot is shown in Fig. 7. The joint torques from the inverse dynamics of the robot are obtained as

$$\boldsymbol{\tau}_\theta = \boldsymbol{I}_{0\theta}^T\ddot{\boldsymbol{q}}_0 + \boldsymbol{I}_\theta\ddot{\boldsymbol{q}}_\theta + \boldsymbol{c}_\theta - \boldsymbol{\tau}_{e_\theta}. \tag{40}$$

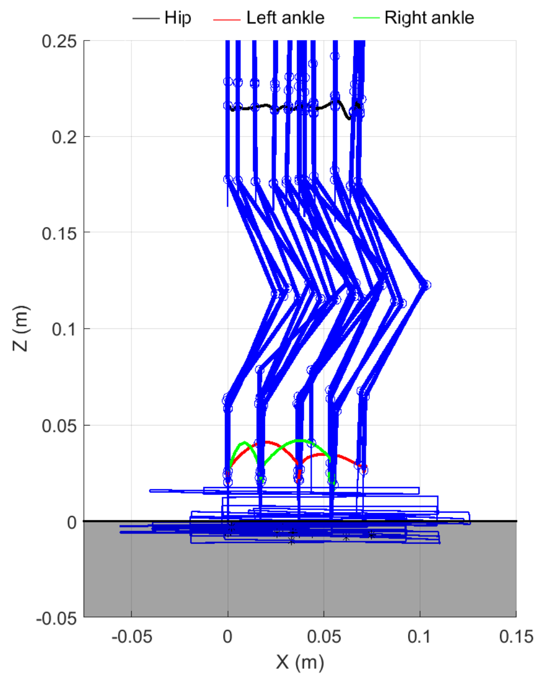

Fig. 7: Simulation of the robot walking on deformable terrain in sagittal plane

The joint torques of the legs are shown in Fig. 8. The comparison of the simulated and desired trajectory of the COM on deformable terrain is shown in Fig. 9. The COM trajectory on deformable terrain deviates from the desired due to the rotation of the foot. This is mainly due to the angular momentum of the legs, which is not included in the simplified dynamics model. In Fig. 10, the simulated and desired trajectory of the COM on hard terrain is plotted. The roll and pitch, i.e., the rotation of the foot about the $x-$axis and $y-$axis for walking on deformable and hard terrain are shown in Fig. 11. For smaller step lengths, the velocity component of the COM in the y-direction is significantly higher compared to the x-direction, which causes higher rotation of the foot about the x-axis on deformable terrain. The rotation of the foot and COM trajectory tracking error for walking on deformable terrain can be reduced by using the upper body motion for angular momentum control.

4.1 Experimental results

The proposed method is validated using a 17-DOF Kondo KHR-3HV humanoid robot with KRS-2552RHV servo motors [27]. The robot has five servo motors in each leg, which are utilized for walking, and the remaining seven servo motors of the upper body are locked. The maximum torque capacity of the motor is $1.373\,\mathrm{N-m}$ and the maximum speed is $7.48\,\mathrm{rad/s}$. The servo motors are controlled by RCB-4HV controller

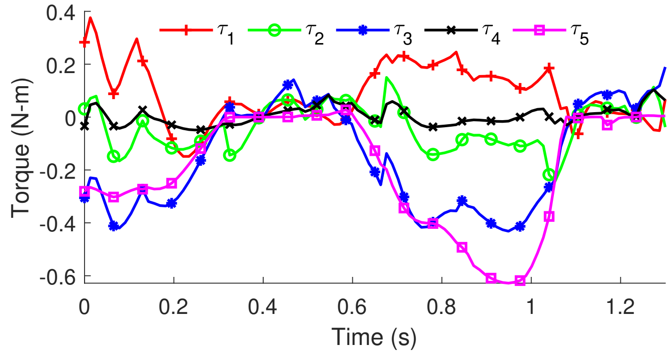

(a) Joint torques of left leg

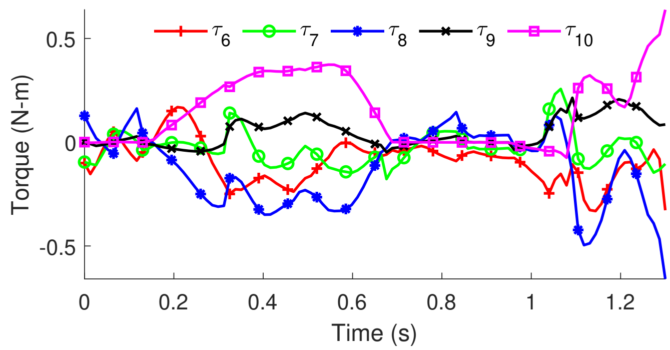

(b) Joint torques of right leg

Fig. 8: Joint torques of the leg joints

board and HeartToHeart4 (HTH4) motion creation software. The communication standard for controlling servo motors with the control board and changing the servo motor settings is ICS (Interactive Communication System).

For deformable terrain, the polyurethane (PU) foam sheet of density $16\,\mathrm{kg/m^3}$ is used. The deformation of the terrain in the SSP due to the self-weight is shown in Fig. 12. In the figure, the left leg foot is statically supporting the weight of the robot, whereas the right leg foot is lifted to show the terrain deformation of approximately 6 mm. To demonstrate walking with joint angle trajectories shown in Fig. 6, the servo motion command data is generated by RCB-4 python library ‘rcb4lib’. The extensible markup language (XML) motion file is written to the robot controller (RCB-4HV) by HTH4 software. The robot’s motion is recorded at a frame rate of 30 fps with 1080p resolution. The extracted video frames of the robot walking on the deformable terrain are shown in Fig. 13. The reflective markers are attached to the hip and both feet of the robot to record the trajectories using the motion capture system (frame rate of $147\,\mathrm{Hz}$). The desired, simulated and experimental trajectories of the hip and leg ankles are shown in Fig. 14. The maximum lift of the swing leg ankle is lower than the desired due to rotation of the stance leg foot on deformable terrain.

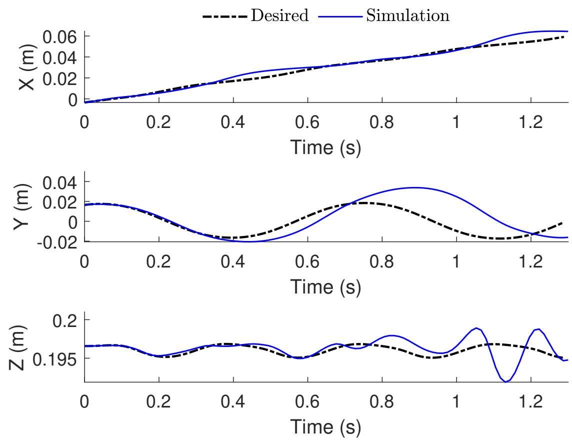

Fig. 9: Desired and simulation trajectory of the COM on deformable terrain

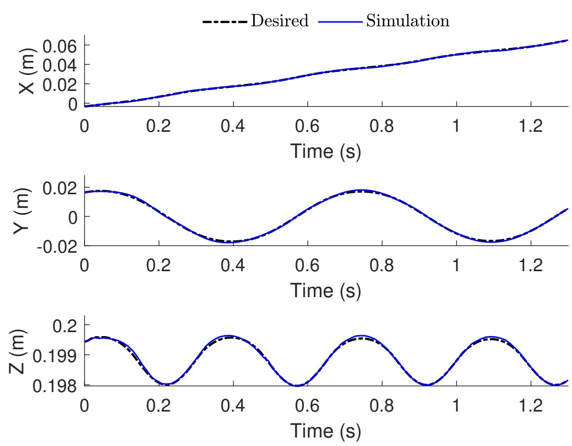

Fig. 10: Desired and simulation trajectory of the COM on hard terrain

This stance leg foot rotation also causes back and forth hip motion. However, the foot placement positions of the swing leg ankle are tracked accurately, and the robot successfully walked on deformable terrain using the proposed method.

The joint trajectories for robot walking on hard terrain are also generated. The video of the robot walking on hard terrain is recorded, and the frames extracted are shown in Fig. 15. The hip and leg ankle trajectories are shown in Fig. 16. The desired hip trajectory is followed in the experiment, which is evident from the figure. The footstep length of the swing leg ankle in the experiment is observed to be higher as compared with the simulation due to gear backlash.

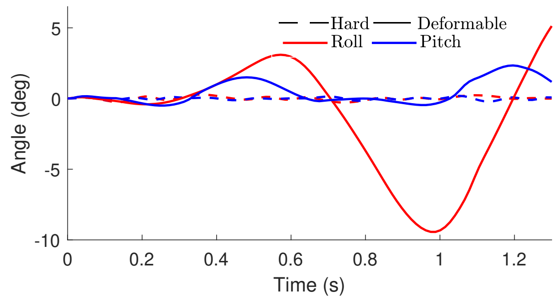

Fig. 11: Foot rotation angle about $x-$axis (roll) and $y-$axis (pitch) on deformable and hard terrain

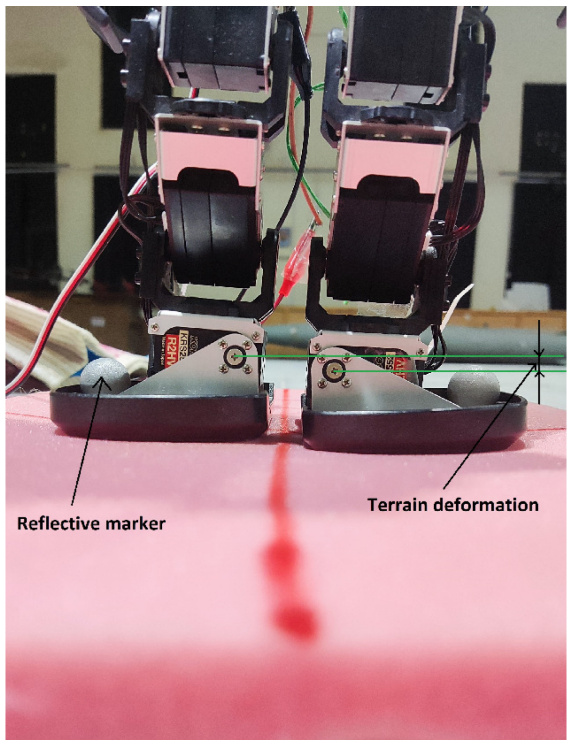

Fig. 12: Terrain deformation due to self-weight of the robot

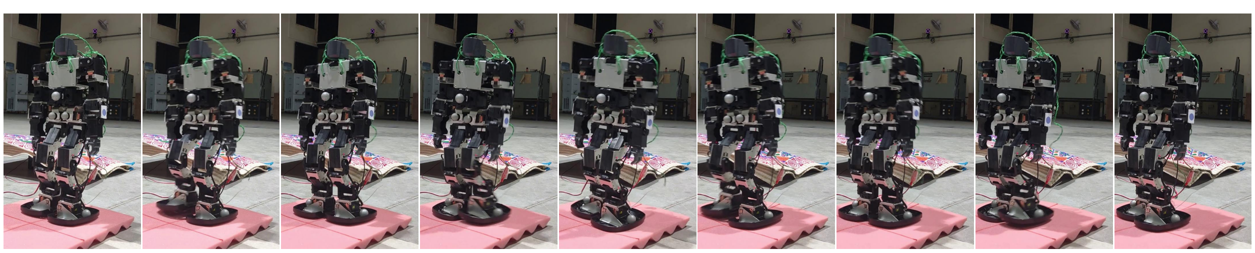

Fig. 13: Snapshots of Kondo KHR-3HV humanoid robot walking forward on deformable terrain

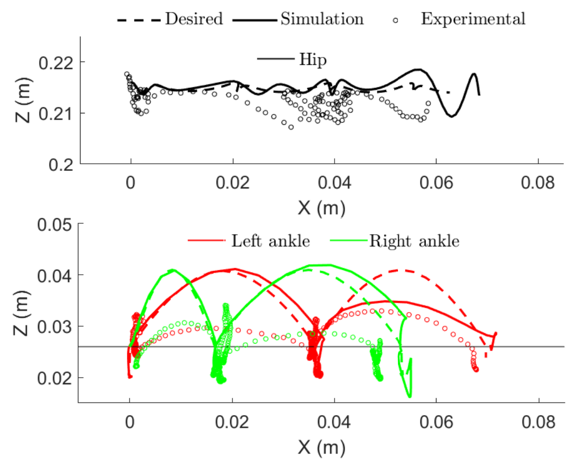

Fig. 14: Hip and ankle trajectories on deformable terrain

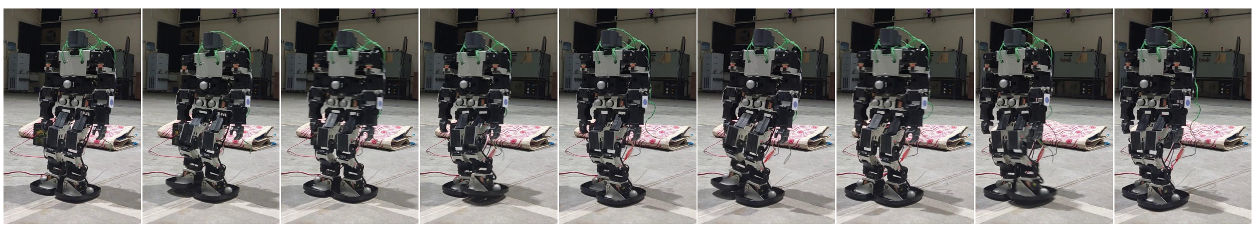

Fig. 15: Snapshots of Kondo KHR-3HV humanoid robot walking forward on hard terrain

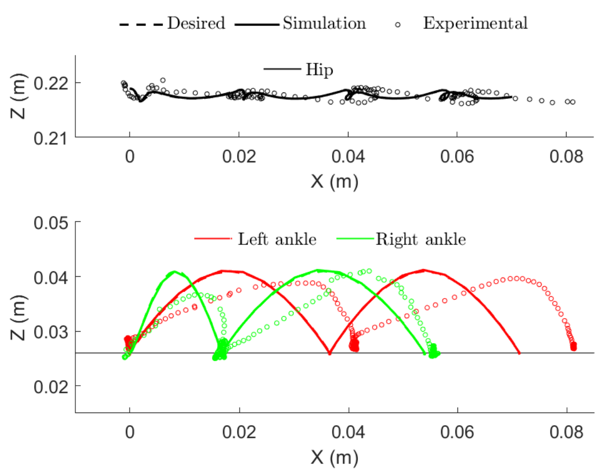

Fig. 16: Hip and ankle trajectories on hard terrain

5 CONCLUSIONS

In this paper, the gait generation of a 10-DOF humanoid robot on deformable terrain is presented. In the single support phase, the dynamics is simplified as the spherical inverted pendulum model, and the double support phase is modeled as the suspended nonlinear pendulum. The motion of the SIP model is used to generate the joint trajectories. The floating-base dynamics is simulated for walking on deformable terrain. In order to validate the proposed method, Kondo KHR-3HV humanoid robot's walking on a deformable polyurethane foam sheet of $16\,\mathrm{kg/m^3}$ density is demonstrated. Desired, simulated and experimental trajectories of the hip and the leg ankles are analyzed. The humanoid robot can walk on flat deformable terrain with known foot-terrain contact parameters. However, the humanoid robot may have to walk on uneven deformable terrain with unknown foot-terrain interaction parameters. The proposed method of leg transition with finite DSP can be extended to parameter identification in the DSP. In future work, the robot's kinematic constraints will also be included in the proposed leg transition for feasible motion on unstructured outdoor terrain.

ACKNOWLEDGEMENTS

The authors would like to thank Dr. Abhishek, Department of Aerospace Engineering, IIT Kanpur for providing access to the motion capture system in the helicopter laboratory and Mr. Prateek Priyaranjan Pradhan for the help in carrying out the experiments.

REFERENCES

[1] Sugihara, T., Nakamura, Y., and Inoue, H., 2002. "Real-time humanoid motion generation through zmp manipulation based on inverted pendulum control". In Proceedings 2002 IEEE International Conference on Robotics and Automation (Cat. No. 02CH37292), Vol. 2, IEEE, pp. 1404–1409.

[2] Choi, Y., Kim, D., Oh, Y., and You, B.-J., 2007. "Posture/walking control for humanoid robot based on kinematic resolution of com jacobian with embedded motion". *IEEE Transactions on Robotics,* **23**(6), pp. 1285–1293.

[3] Sarkar, A., and Dutta, A., 2019. "Optimal trajectory generation and design of an 8-dof compliant biped robot for walk on inclined ground". *Journal of Intelligent & Robotic Systems,* **94**(3), pp. 583–602.

[4] Sato, T., Sakaino, S., Ohashi, E., and Ohnishi, K., 2010. "Walking trajectory planning on stairs using virtual slope for biped robots". *IEEE transactions on industrial electronics,* **58**(4), pp. 1385–1396.

[5] Kuindersma, S., Deits, R., Fallon, M., Valenzuela, A., Dai, H., Permenter, F., Koolen, T., Marion, P., and Tedrake, R., 2016. "Optimization-based locomotion planning, estimation, and control design for the atlas humanoid robot". *Autonomous robots,* **40**(3), pp. 429–455.

[6] Sygulla, F., and Rixen, D., 2020. "A force-control scheme for biped robots to walk over un-

even terrain including partial footholds". *International Journal of Advanced Robotic Systems,* **17**(1), p. 1729881419897472.

[7] Gong, Y., and Grizzle, J. W., 2022. "Zero dynamics, pendulum models, and angular momentum in feedback control of bipedal locomotion". *Journal of Dynamic Systems, Measurement, and Control,* **144**(12), p. 121006.

[8] Zheng, Y. F., Wang, H., Li, S., Liu, Y., Orin, D., Sohn, K., Jun, Y., and Oh, P., 2013. "Humanoid robots walking on grass, sands and rocks". In 2013 IEEE Conference on Technologies for Practical Robot Applications (TePRA), IEEE, pp. 1–6.

[9] Kolvenbach, H., Bellicoso, D., Jenelten, F., Wellhausen, L., and Hutter, M., 2018. "Efficient gait selection for quadrupedal robots on the moon and mars". In 14th International Symposium on Artificial Intelligence, Robotics and Automation in Space (i-SAIRAS 2018), ESA Conference Bureau.

[10] Hashimoto, K., Kang, H.-j., Nakamura, M., Falotico, E., Lim, H.-o., Takanishi, A., Laschi, C., Dario, P., and Berthoz, A., 2012. "Realization of biped walking on soft ground with stabilization control based on gait analysis". In 2012 IEEE/RSJ International Conference on Intelligent Robots and Systems, IEEE, pp. 2064–2069.

[11] Mesesan, G., Englsberger, J., Garofalo, G., Ott, C., and Albu-Schäffer, A., 2019. "Dynamic walking on compliant and uneven terrain using dcm and passivity-based whole-body control". In 2019 IEEE-RAS 19th International Conference on Humanoid Robots (Humanoids), IEEE, pp. 25–32.

[12] Ding, L., Gao, H., Deng, Z., Song, J., Liu, Y., Liu, G., and Iagnemma, K., 2013. "Foot–terrain interaction mechanics for legged robots: Modeling and experimental validation". *The International Journal of Robotics Research,* **32**(13), pp. 1585–1606.

[13] Gora, S., Gupta, S. S., and Dutta, A., 2021. "Optimal gait generation of an 8-dof biped robot on deformable terrain using floating-base dynamics". In Advances in Robotics-5th International Conference of The Robotics Society, pp. 1–6.

[14] Xiong, X., Ames, A. D., and Goldman, D. I., 2017. "A stability region criterion for flat-footed bipedal walking on deformable granular terrain". In 2017 IEEE/RSJ International Conference on Intelligent Robots and Systems (IROS), IEEE, pp. 4552–4559.

[15] Kajita, S., Kanehiro, F., Kaneko, K., Yokoi, K., and Hirukawa, H., 2001. "The 3d linear inverted pendulum mode: A simple modeling for a biped walking pattern generation". In Proceedings 2001 IEEE/RSJ International Conference on Intelligent Robots and Systems. Expanding the Societal Role of Robotics in the the Next Millennium (Cat. No. 01CH37180), Vol. 1, IEEE, pp. 239–246.

[16] Shibuya, M., Suzuki, T., and Ohnishi, K., 2006. “Trajectory planning of biped robot using linear pendulum mode for double support phase”. In IECON 2006-32nd Annual Conference on IEEE Industrial Electronics, IEEE, pp. 4094–4099.

[17] Xie, Z., Li, L., and Luo, X., 2021. “Three-dimensional aperiodic biped walking including the double support phase using lipm and lpm”. *Robotics and Autonomous Systems,* **143**, p. 103831.

[18] Crews, S., and Travers, M., 2020. “Energy management through footstep selection for bipedal robots”. *IEEE Robotics and Automation Letters,* **5**(4), pp. 5485–5493.

[19] Gora, S., Gupta, S. S., and Dutta, A., 2023. “Energy-based footstep planning of biped on uneven deformable terrain using nonlinear inverted pendulum”. *Journal of Mechanisms and Robotics,* **15**(5).

[20] McGeer, T., 1990. “Passive dynamic walking”. *Int. J. Robotics Res.,* **9**(2), pp. 62–82.

[21] Shah, S. V., Saha, S. K., and Dutt, J. K., 2013. “Dynamics of tree-type robotic systems”. In *Dynamics of Tree-Type Robotic Systems*. Springer, pp. 73–88.

[22] Mummolo, C., Peng, W. Z., Gonzalez, C., and Kim, J. H., 2018. “Contact-dependent balance stability of biped robots”. *Journal of Mechanisms and Robotics,* **10**(2), p. 021009.

[23] Gora, S., Gupta, S. S., and Dutta, A., 2023. “Gait generation of 6-dof biped robot on inclined deformable terrain using nonlinear inverted pendulum”. In Proceedings of the 2023 6th International Conference on Advances in Robotics, pp. 1–6.

[24] Tsuji, T., and Ohnishi, K., 2002. “A control of biped robot which applies inverted pendulum mode with virtual supporting point”. In 7th International Workshop on Advanced Motion Control. Proceedings (Cat. No. 02TH8623), IEEE, pp. 478–483.

[25] Ge, C., and Rice, B., 2018. “Impact damping ratio of a nonlinear viscoelastic foam”. *Polymer Testing,* **72**, pp. 187–195.

[26] Sugihara, T., and Nakamura, Y., 2002. “Whole-body cooperative balancing of humanoid robot using cog jacobian”. In IEEE/RSJ international conference on intelligent robots and systems, Vol. 3, IEEE, pp. 2575–2580.

[27] Kondo KHR-3HV humanoid robot. `https://kondo-robot.com/`. Accessed: Nov. 01, 2023.

APPENDIX A: EXPRESSION OF MATRICES IN EQUATIONS OF MOTION OF SIP MODEL

$$\boldsymbol{I}_p = \begin{bmatrix} m, & 0, & 0, & 0, & ml\cos\theta_y, \\ 0, & m, & 0, & -ml\cos\theta_x\cos\theta_y, & ml\sin\theta_x\sin\theta_y, \\ 0, & 0, & m, & -ml\cos\theta_y\sin\theta_x, & -ml\cos\theta_x\sin\theta_y, \\ 0, & -ml\cos\theta_x\cos\theta_y, & -ml\cos\theta_y\sin\theta_x & I_{xx}+ml^2\cos^2\theta_y, & I_{xy}\cos\theta_x + I_{xz}\sin\theta_x, \\ ml\cos\theta_y, & ml\sin\theta_x\sin\theta_y, & -ml\cos\theta_x\sin\theta_y, & I_{xy}\cos\theta_x + I_{xz}\sin\theta_x, & \begin{matrix} I_{yy}\cos^2\theta_x + I_{zz}\sin^2\theta_x \\ +2I_{yz}\cos\theta_x\sin\theta_x + ml^2 \end{matrix} \end{bmatrix}, \tag{41}$$

$$\boldsymbol{c}_p = \begin{bmatrix} -ml\dot{\theta_y}^2\sin\theta_y, \\ \\ ml\dot{\theta_y}(\dot{\theta_x}\cos\theta_x\sin\theta_y + \dot{\theta_y}\cos\theta_y\sin\theta_x), \\ \\ m(-l\dot{\theta_y}^2\cos\theta_x\cos\theta_y + l\dot{\theta_x}\dot{\theta_y}\sin\theta_x\sin\theta_y + g), \\ \\ 2I_{yz}\dot{\theta_y}^2\cos^2\theta_x - I_{yz}\dot{\theta_y}^2 - (I_{yy}\dot{\theta_y}^2\sin(2\theta_x))/2 + (I_{zz}\dot{\theta_y}^2\sin 2\theta_x)/2 \\ +I_{xz}\dot{\theta_x}\dot{\theta_y}\cos\theta_x - I_{xy}\dot{\theta_x}\dot{\theta_y}\sin\theta_x - mgl\cos\theta_y\sin\theta_x - ml^2(\dot{\theta_x}\dot{\theta_y}\sin 2\theta_y)/2, \\ \\ I_{xy}\dot{\theta_x}^2\sin\theta_x - I_{xz}\dot{\theta_x}^2\cos\theta_x + I_{yz}\dot{\theta_x}\dot{\theta_y} - 2I_{yz}\dot{\theta_x}\dot{\theta_y}\cos^2\theta_x \\ +(I_{yy}\dot{\theta_x}\dot{\theta_y}\sin 2\theta_x)/2 - (I_{zz}\dot{\theta_x}\dot{\theta_y}\sin 2\theta_x)/2 - mgl\cos\theta_x\sin\theta_y \end{bmatrix}, \tag{42}$$

$$\boldsymbol{J}_p = \begin{bmatrix} 1,\ 0,\ 0,\ 0,\ 0 \\ 0,\ 1,\ 0,\ 0,\ 0 \\ 0,\ 0,\ 1,\ 0,\ 0 \end{bmatrix}. \tag{43}$$

LIST OF FIGURES

LIST OF TABLES